

Propagation properties of the average intensity evolution of Whittaker–Gaussian beams in oceanic turbulence

N. Nossir^{1, 2}, L. Dalil-Essakali¹ and A. Belafhal¹ *

¹Laboratory LPNAMME, Laser Physics Group, Department of Physics, Faculty of Sciences, Chouaïb Doukkali University, P. B 20, 24000 El Jadida, Morocco,

²Laboratory LEST, Applied Sciences and Didactics Group, Higher School of Education and Training of Berrechid, Hassan 1st University, P. B 539 Settat, Morocco

*Corresponding author: belafhal@gmail.com

ABSTRACT

This study investigates the propagation behavior of a class of general circular light beams (CiBs), known as Whittaker–Gaussian beams (WGBs), as they traverse oceanic turbulence by employing the Rytov approximation and diffraction integral formalism. Based on the derived analytical expression, numerical simulations were performed to evaluate the impact of oceanic turbulence on the axial intensity distribution of these circular beams. The results indicate that the beam intensity profile is significantly influenced by variations in its initial parameters, namely, the beam waist and wavelength, as well as by key oceanic turbulence parameters, including the rate of mean-square temperature dissipation, balance between temperature and salinity fluctuations, and rate of turbulent kinetic energy dissipation per unit mass. These findings offer deeper insights that can support the development and optimization of optical systems used in underwater communication, remote sensing, and imaging applications.

ARTICLE INFO

Keywords:

Circular light beams, Whittaker–Gaussian beams, Oceanic turbulence, Rytov approximation theory, Diffraction integral formalism, Remote sensing.

Article History:

Received: 08-October-2025,

Revised: 03-December-2025,

Accepted: 10-December-2025,

Available online: 28 December 2025.

1. INTRODUCTION

In recent years, extensive research has focused on the propagation of laser beams in optical systems [1–8]. The increasing use of laser beams, particularly in atmospheric optics, has intensified interest in understanding how light propagates through turbulent environments. Consequently, the study of laser beam propagation under atmospheric turbulence has become a key topic in optical research. Atmospheric turbulence, characterized by irregular fluid motion, has attracted significant attention owing to its importance in applications such as laser communication, remote sensing, laser weapon systems, lattice spectroscopy, tracking, optical coherence tomography, and atmospheric laser wireless communication [9–14]. When a laser beam propagates through a turbulent medium, it experiences several effects, including beam spreading (divergence), beam wander (positional

jitter), intensity fluctuations, and wavefront distortions, which can degrade the system performance and limit technological progress. Consequently, studying random fluctuations in media, such as biological tissues and atmospheric turbulence, is essential. Numerous studies have examined the behavior of different types of laser beams in a wide range of turbulent environments [15–23].

Similarly, another random medium that can significantly influence a beam's propagation characteristics is oceanic turbulence, which has attracted research interest in various fields since the early 20th century. Accordingly, scientists are currently investigating the propagation of laser beams in this challenging medium. Owing to its complexity, oceanic turbulence has been less explored than atmospheric turbulence. Nonetheless, specific difficulties and practical applications associated with optical



propagation in oceanic environments have reinforced its relevance as a research topic. Thus, several researchers have focused on how temperature and salinity fluctuations affect laser beam propagation, including the degree of polarization and scintillation index.

In recent years, many theoretical and experimental studies have examined the behavior of different types of laser beams in oceanic turbulence [16–41]. On the other hand, this type of beam structure is recognized as a significant optical beam owing to its distinctive features and versatile configuration and is referred to as the Whittaker–Gaussian beam. This represents a general solution to the equation for paraxial waves in circular cylindrical coordinates [42]. These properties form an additional category of standard circular beams [43], and can be described using Whittaker and confluent hypergeometric functions. Because of its structural flexibility and broad applicability, this beam has attracted considerable research interest. For instance, studies have examined the radiation forces exerted by Whittaker–Gaussian beams and their propagation through gradient-index media and turbulent environments [44–46]. The purpose of this study is to explore how the characteristics of a special case of general CiBs change as they travel across oceanic turbulence. To the best of our knowledge, the spreading behavior of this class of beams in such a medium has not been previously investigated. The remainder of this paper is organized as follows: Section 2 presents the mathematical definition of the incident beam and examines its behavior after passing through oceanic turbulence based on the Huygens–Fresnel diffraction integral. Section 3 provides a numerical analysis of the beam intensity distribution and propagation characteristics in oceanic turbulence, and Section 4 highlights the key conclusions of this study.

2. THEORETICAL ANALYSIS OF THE PROPAGATION OF WGBS IN AN OCEANIC TURBULENCE ENVIRONMENT

In the cylindrical coordinate system, the mathematical expression for the input beam at $z = 0$ can be written as follows [42]:

$$E_{in}(r_1, \theta_1) = \left(\frac{ir_1^2}{2\omega_0^2}\right)^{-1/2} M_{\frac{\vartheta}{2}, \frac{s}{2}} \left(\frac{ir_1^2}{2\omega_0^2}\right) \exp\left(-\frac{r_1^2}{\omega_0^2}\right) \times \exp(is\theta_1). \tag{1}$$

In this equation, r and ϕ are the coordinates of the cylindrical system, s is the beam order, ω_0 is the Gaussian part radius, and ϑ indicates a beam-related parameter.

Recalling the following expression, which connects the Kummer function and $M_{\frac{\vartheta}{2}, \frac{s}{2}}(X)$, the hypergeometric

function ${}_1F_1(\cdot)$ is [47]:

$$M_{\frac{\vartheta}{2}, \frac{s}{2}}(X) = X^{\frac{s}{2} + \frac{1}{2}} \exp\left(-\frac{X}{2}\right) \times {}_1F_1\left(\frac{s - \vartheta + 1}{2}, s + 1; X\right). \tag{2}$$

and utilizing the confluent hypergeometric function in its series-expansion form

$${}_1F_1(c, d, w) = \sum_{b=0}^{\infty} \frac{(c)_b}{(d)_b} \frac{w^b}{b!}, \tag{3}$$

Equation (1) can be rewritten as

$$E_{in}(r_1, \theta_1) = \left(\frac{ir^2}{2\omega_0^2}\right)^{\frac{s}{2}} \exp\left(-\frac{4+i}{4\omega_0^2} r^2\right) \times \sum_{m=0}^{\infty} \frac{\left(\frac{s+1-\vartheta}{2}\right)_m}{(s+1)_m} \frac{\left(\frac{ir^2}{2\omega_0^2}\right)^m}{m!} \times \exp(is\phi). \tag{4}$$

This equation represents the incident field of a beam structure. It is expressed as the product of an infinite summation and Gaussian beam. When $m = 0$, the beam contains no vortices and is reduced to a standard Gaussian beam. The normalized intensity distribution of the incident beam is shown in three dimensions in Fig. 1. It shows how this beam behaves for various beam order values of ($s = 1$ and $s = 4$) with a variety of incident beam waists ($\omega_0 = 1$, $\omega_0 = 3$, and $\omega_0 = 4$). The graphs show that the center of the beam exhibited a hollow profile with zero intensity. Moreover, it can be observed that the primary dark region expands toward higher values in the x – y coordinate system as both the beam order and beam radius increase. This indicates that the distinctive features of this class of CiBs give it a particular profile that is relevant to laser physics and may be useful for manipulating and confining small particles. The phase distributions for the two values of beam order and three values of beam radius are shown in Fig. 2. It was observed that with increasing ω_0 from 1 to 6, the phase structure changes and becomes more noticeable. Additionally, the graphs show a vertically antisymmetric phase distribution of the beam, which occurs in the odd modes. Owing to its hollow structure, this beam possesses significant scientific value and may have applications in various areas of physics.

Consequently, as the beam order increased, the spiral phase structure became more divergent. The spiral phase pattern is more convergent at low beam orders and becomes increasingly divergent as the beam order increases. In addition, the spiral phase structure rotated clockwise.

The following section examines the propagation of a special case of general CiBs along the z -axis in an oceanic turbulent medium, using cylindrical coordinates. This propagation originates from the incident field at $z = 0$,

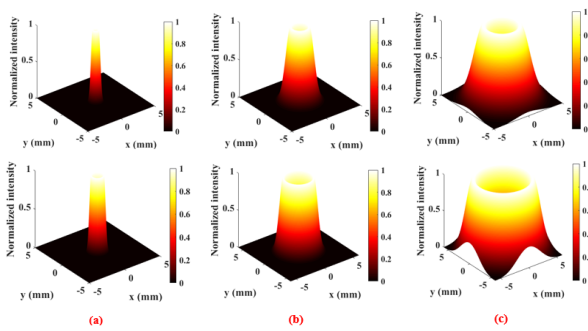


Figure 1. The 3D normalized intensity in the x, y-directions at the incident plane of the of a kind of CiBs, with $\vartheta = 1$. For (a) $\omega_0 = 1\text{mm}$, (b) $\omega_0 = 3\text{mm}$, and (c) $\omega_0 = 6\text{mm}$. Top row ($s = 1$) and bottom row ($s = 4$).

as shown in Fig. 3, and is modeled using the extended Huygens–Fresnel diffraction integral.

The average intensity at the receiving plane can be expressed as [9]

$$\begin{aligned} \langle I_{\text{out}}(\vec{\rho}, z) \rangle &= \left(\frac{k}{2\pi z} \right)^2 \int_0^{+\infty} \int_0^{+\infty} \int_0^{2\pi} \int_0^{2\pi} \\ \langle E_{\text{in}}(\vec{r}_1, 0) E_{\text{in}}^*(\vec{r}_2, 0) \rangle & \\ &\times \exp \left[\frac{ik}{2z} \left((\vec{r}_1 - \vec{\rho})^2 - (\vec{r}_2 - \vec{\rho})^2 \right) \right] \\ &\times \langle \exp[\psi(r_1, \rho) + \psi^*(r_2, \rho)] \rangle d\vec{r}_1 d\vec{r}_2 \end{aligned} \quad (5)$$

The complex conjugate is denoted by $*$, $\langle \cdot \rangle$ represents the ensemble average, where the wave number is $k = 2\pi/\lambda$, λ is the wavelength of the beam, and $\psi(r_1, \rho)$ symbolizes the phase disturbance and random fluctuations induced by the oceanic turbulent medium. Mean term of the oceanic turbulence ensemble [9]

$$\begin{aligned} \langle \exp[\psi(r_1, \rho) + \psi^*(r_2, \rho)] \rangle &= \exp \left[-\frac{1}{2} D_{\Psi}(r_1, r_2, \rho) \right] \\ &= \exp \left[\frac{2r_1 r_2}{\rho_0^2} \cos(\theta_1 - \theta_2) \right] \exp \left[-\frac{r_1^2 + r_2^2}{\rho_0^2} \right]. \end{aligned} \quad (6)$$

where D_{Ψ} is the wave assembly function of the random complex phase in the Rytov symbol.

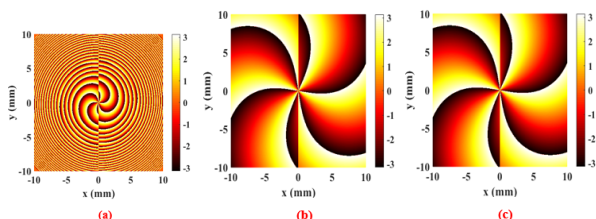


Figure 2. The phase distributions of the incident beam for (a) $\omega_0 = 1\text{mm}$, (b) $\omega_0 = 3\text{mm}$, and (c) $\omega_0 = 6\text{mm}$ with $\vartheta = 1$ and ($s = 1$).

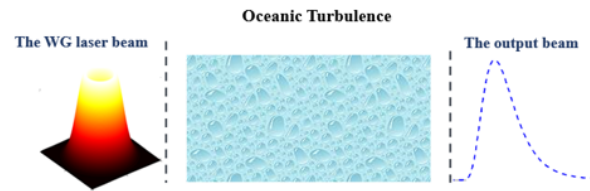


Figure 3. Illustration of the structure of the studied type of CiBs as it propagates through oceanic turbulence.

In this equation, ρ_0 represents the lateral coherence of a spherical wave. This can be calculated as follows:.

$$\rho_0 = \left[\frac{\pi^2}{3} k^2 z \int_0^{\infty} \kappa^3 \Phi(\kappa) d\kappa \right]^{-1/2}, \quad (7)$$

where κ is the magnitude of the spatial frequency $\Phi(\kappa)$ characterizes the fluctuations in the spatial power spectrum of the refractive index in oceanic turbulence. A spatial power–spectrum model for refractive-index fluctuations in oceanic turbulence was established for an isotropic yet inhomogeneous seawater medium.

This model accounts for the differing eddy diffusivities of temperature and salinity in seawater, and is expressed as follows [48]:

$$\Phi(\kappa) = 0.388 \times 10^{-8} \overline{\epsilon}^{-11/3} \left[1 + 2.35 (\kappa\eta)^{2/3} \right] f(\kappa, \zeta, \chi_T), \quad (8.1)$$

where,

$$\begin{aligned} f(\kappa, \zeta, \chi_T) &= \frac{\chi_T}{\zeta^2} \left[\zeta^2 \exp(-A_T \delta) \right. \\ &\left. + \exp(-A_S \delta) - 2\zeta \exp(-A_{TS} \delta) \right]. \end{aligned} \quad (8.2)$$

where $\overline{\epsilon}$ represents the dissipation rate of kinetic energy per unit mass of fluid, with typical values ranging from $10^{-10} \text{m}^2 \text{s}^{-3}$ to $10^{-1} \text{m}^2 \text{s}^{-3}$; the Kolmogorov microscale (inner scale) is denoted η and has a typical value of 10^{-3}m ; χ_T indicates the dissipation rate of the mean-squared temperature, which falls within the range $10^{-4} \text{K}^2 \text{s}^{-1}$ to $10^{-10} \text{K}^2 \text{s}^{-1}$; and ζ defines the ratio of temperature- and salinity-induced contributions to the refractive-index spectrum, taking values in the interval $[-5, 0]$, with the values -5 and corresponding to temperature-induced and salinity-induced optical fluctuations, respectively. The constants have specific numerical values, $A_T = 1.863 \times 10^{-2}$, $A_S = 1.9 \times 10^{-4}$, $A_{TS} = 9.41 \times 10^{-3}$, and $\delta = 8.284(\kappa\eta)^{4/3} + 12.978(\kappa\eta)^2$ where where κ is the spatial frequency associated with the microscale.

By substituting Eq. 1 into Eq. 5, the intensity of the studied beam propagating through oceanic turbulence can be expressed η .



$$\begin{aligned} \langle I_{out}(\rho, z) \rangle &= \left(\frac{k}{2z\pi}\right)^2 \sum_{m_1=0}^{\infty} \frac{\left(\frac{s+1-\theta}{2}\right)_{m_1}}{(s+1)_{m_1}} \frac{\left(\frac{i}{2\omega_0^2}\right)^{\frac{s}{2}+m_1}}{m_1!} \\ &\times \sum_{m_2=0}^{\infty} \frac{\left(\frac{s+1-\theta}{2}\right)_{m_2}}{(s+1)_{m_2}} \frac{\left(\frac{-i}{2\omega_0^2}\right)^{\frac{s}{2}+m_2}}{m_2!} \\ &\times \int_0^\infty \int_0^\infty \int_0^{2\pi} \int_0^{2\pi} e^{is(\theta_1-\theta_2)} \\ &\times \exp\left[\frac{ik}{z}\rho\left(r_1 \cos(\theta_1-\psi) - r_2 \cos(\theta_2-\psi)\right)\right] \\ &\times \exp(-\alpha_2 r_2^2) \exp\left[\frac{2r_1 r_2}{\rho_0^2} \cos(\theta_1-\theta_2)\right] \exp(-\alpha_1 r_1^2) \\ &\times r_1^{s+2m_1+1} r_2^{s+2m_2+1} dr_1 d\theta_1 dr_2 d\theta_2. \end{aligned} \quad (9)$$

where

$$\alpha_1 = \frac{1}{\omega_0^2} + \frac{1}{\rho_0^2} - \frac{ik}{2z} - i\frac{1}{4\omega_0^2}, \quad (10a)$$

and

$$\alpha_2 = \frac{1}{\omega_0^2} + \frac{1}{\rho_0^2} + \frac{ik}{2z} + i\frac{1}{4\omega_0^2}. \quad (10b)$$

With the use of the finite integral given by [49]

$$\begin{aligned} \int_0^{2\pi} \exp(-im\theta_1 + x \cos(\theta_1 - \theta_2)) d\theta_1 \\ = 2\pi \exp(-im\theta_2) I_m(x), \end{aligned} \quad (11)$$

where I_m illustrates the first sort of modified Bessel function of order m and after some rearrangements, Eq.9 becomes

$$\begin{aligned} \langle I_{out}(\rho, z) \rangle &= \left(\frac{2\pi k}{z}\right)^2 \sum_{m_1=0}^{\infty} \frac{\left(\frac{s+1-\theta}{2}\right)_{m_1}}{(s+1)_{m_1}} \frac{\left(\frac{i}{2\omega_0^2}\right)^{\frac{s}{2}+m_1}}{m_1!} \\ &\sum_{m_2=0}^{\infty} \frac{\left(\frac{s+1-\theta}{2}\right)_{m_2}}{(s+1)_{m_2}} \frac{\left(\frac{-i}{2\omega_0^2}\right)^{\frac{s}{2}+m_2}}{m_2!} \\ &\times \int_0^{+\infty} I_s\left(\frac{2r_1}{\rho_0}\right) \\ &\exp(-\alpha_2 r_2^2) r_1^{s+2m_1+1} dr_1 \int_0^{+\infty} \exp(-\alpha_1 r_1^2) \\ &I_s\left(\frac{2r_2}{\rho_0}\right) r_2^{s+2m_2+1} dr_2, \end{aligned} \quad (12)$$

The following equality is recalled as [50]

$$\begin{aligned} \int_0^\infty x^{\mu-\frac{1}{2}} \exp(-\alpha x) I_{2\nu}(2\beta\sqrt{x}) dx &= \frac{\Gamma(\mu+\nu+\frac{1}{2})}{\Gamma(2\nu+1)} \\ \beta^{-1} e^{\frac{\beta^2}{2\alpha}} \alpha^{-\mu} M_{-\mu, \nu}\left(\frac{\beta^2}{\alpha}\right), \end{aligned} \quad (13)$$

$$\left[Re\left(\mu + \mu + \frac{1}{2}\right)\right] > 0$$

where $\Gamma(x)$ is a function of gamma. By using the Eq.2, which is expressed in Eq. 13 from the Kummer function as a function of the hypergeometric function ${}_1F_1(\cdot)$, and

employed to resolve the integral of Eq. 12 [47]:

$$\begin{aligned} \langle I_{out}(0, z) \rangle &= \left(\frac{k}{z}\right)^2 \frac{\left(\frac{1}{\rho_0}\right)^s}{2\Gamma(s+1)} \sum_{m_1=0}^{\infty} \frac{\left(\frac{s+1-\theta}{2}\right)_{m_1}}{(s+1)_{m_1}} \frac{\left(\frac{i}{2\omega_0^2}\right)^{\frac{s}{2}+m_1}}{m_1!} \\ &\sum_{m_2=0}^{\infty} \frac{\left(\frac{s+1-\theta}{2}\right)_{m_2}}{(s+1)_{m_2}} \frac{\left(\frac{-i}{2\omega_0^2}\right)^{\frac{s}{2}+m_2}}{m_2!} \\ &\times \frac{\Gamma(s+m_2+1)}{a_2^{s+m_2+1}} \int_0^{+\infty} r_1^{2s+2m_1+1} \\ &\exp(-\alpha_1 r_1^2) {}_1F_1\left(s+m_2+1; s+1; \frac{r_1^2}{\rho_0^4 \alpha_2}\right) dr_1. \end{aligned} \quad (14)$$

In addition, the following integral equation can be used:

$$\begin{aligned} \int_0^\infty x^{\delta'-1} \exp(-\mu'x) {}_mF_n(\alpha_1, \alpha_2, \dots, \alpha_m; \gamma_1, \gamma_2, \dots, \gamma_n; \lambda x) dx \\ = \\ \Gamma(\delta') \mu'^{-\delta'} {}_{m+1}F_n\left(\alpha_1, \alpha_2, \dots, \alpha_m; \delta'; \gamma_1, \gamma_2, \dots, \gamma_n; \frac{\lambda}{\mu'}\right), \end{aligned} \quad (15)$$

with $m \leq n, Re(\delta') > 0; Re(\mu') > 0$, if $m < n; Re(\mu') > \lambda$, if $m = n$.

After straightforward algebraic calculations, the output average intensity of this type of general CiB in oceanic turbulence can be expressed as follows:

$$\begin{aligned} \langle I_{out}(0, z) \rangle &= \frac{k^2}{z^2} \frac{\left(\frac{1}{\rho_0}\right)^s}{2^2 \Gamma(s+1)} \sum_{m_1=0}^{\infty} \frac{\left(\frac{s+1-\theta}{2}\right)_{m_1}}{(s+1)_{m_1}} \frac{\left(\frac{i}{2\omega_0^2}\right)^{\frac{s}{2}+m_1}}{m_1!} \\ &\sum_{m_2=0}^{\infty} \frac{\left(\frac{s+1-\theta}{2}\right)_{m_2}}{(s+1)_{m_2}} \frac{\left(\frac{-i}{2\omega_0^2}\right)^{\frac{s}{2}+m_2}}{m_2!} \\ &\times \frac{\Gamma(s+m_2+1)}{a_2^{s+m_2+1}} \frac{\Gamma(s+m_1+1)}{a_1^{s+m_1+1}} \\ &{}_2F_1\left(s+m_2+1, s+m_1+1; s+1; \frac{1}{\rho_0^4 \alpha_1 \alpha_2}\right), \end{aligned} \quad (16)$$

where ${}_2F_1(\cdot)$ denotes the hypergeometric function. After modifying the final expression, Eq. 16 is changed to (see Appendix A)

$$\begin{aligned} \langle I_{out}(0, z) \rangle &= \frac{k^2}{z^2} \frac{\left(\frac{1}{\rho_0}\right)^s}{2^2} \left(\frac{-i}{2\omega_0^2}\right)^{\frac{s}{2}} \left(\frac{i}{2\omega_0^2}\right)^{\frac{s}{2}} \\ &\times \frac{\Gamma(s+1)}{a_1^{s+1} a_2^{s+1}} \\ &\times F_K\left(\frac{s+1-\theta}{2}, s+1, s+1, s+1; \frac{s+1-\theta}{2}, s+1, s+1, s+1; s+1, \frac{i}{2\alpha_1 \omega_0^2}, \frac{-i}{2\alpha_2 \omega_0^2}, \frac{1}{\rho_0^4 \alpha_1 \alpha_2}\right). \end{aligned} \quad (17)$$

where $F_K(\cdot)$ indicates the three variables hypergeo-

metric function The primary outcome of the present study is Eq. 17, which describes the resulting average intensity field of the examined CiBs in an oceanically turbulent environment.

3. NUMERICAL RESULTS AND DISCUSSION

In this section, we employ the closed-form analytical expression in Eq. 17 to perform numerical calculations to evaluate the evolution of the considered beam as it propagates through the oceanic turbulence. The computation parameters were selected as the $\omega_0 = 0.02 m$, $\lambda = 417 nm$. Fig. 4 shows the impact of the mean-square temperature parameter dissipation rate χ_T on the normalized distribution of the CiBs special case intensity in oceanic turbulence for two beam order values. It is evident from the curves that the dark region increases significantly with increasing beam-order s . It is particularly significant in various fields of physics owing to the null intensity at the center of the beam. It is also evident from this illustration that the axial intensity is zero during the first few meters of the propagation distance. Because the beam **loses** its initial black center hollow owing to diffraction and oceanic turbulence, its intensity decreases along the propagation distance. As we moved farther away from this region, the intensity gradually increased until it reached its maximum. In this instance, the intensity is highly concentrated on a large value of the parameter χ_T and under a low propagation distance; similarly, the studied beam decreases faster for a higher χ_T , which suggests that the medium is agitated. As a result, for a broad range of low values of χ_T , the normalized intensity adopts a wider profile in oceanic turbulence, and the beam maintains its hollow characteristic for a longer period of time. It is concluded that the explored beam is more resilient to oceanic turbulence when χ_T takes a small value. This indicates that the beam was not significantly affected by oceanic turbulence in the far-field region.

Fig. 5 presents the normalized intensity of this type of circular beam in oceanic turbulence for various values of oceanic parameters, ζ_r , as a function of propagation distance and beam order. When the beam order and propagation distance increase, the oceanic variable ζ has a significant effect on the intensity of the beam.

From this figure, it is observed that z_{max} increases as the parametric oceanic increases ζ . Moreover, when the beam order was large, the central peak intensity increased more slowly. Therefore, we can conclude that the disappearance of the initial central dark spot slows with increasing s and ζ . This property pertains to atom confinement, making it extremely important. The examined beam is more prominent in terms of axial intensity. As a result, at low values of ζ_r , the beam is more resistant to changes caused by oceanic turbulence.

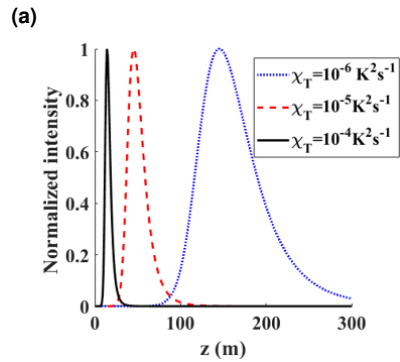
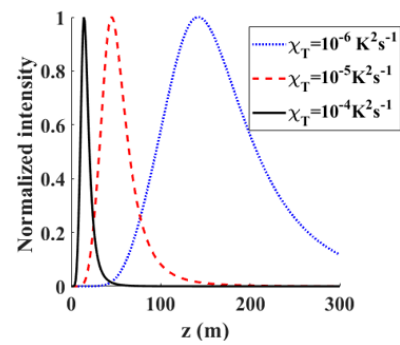


Figure 4. Normalized intensity distribution of a type of WGBs for two values of beam order (a) $s = 0$ and (b) $s = 4$, and diverse values of χ_T , with $\epsilon = 10^{-1} m^2 s^{-3}$ and $\zeta = -1$.

Figure. Six presents the normalized axial intensity distribution of the investigated beam for two beam-order values in a turbulent oceanic environment, considering three values of the dissipation rate of the turbulent kinetic energy per unit mass of fluid. The axial intensity remains nearly unchanged near zero at the beginning of the propagation until it reaches its maximum value, as displayed in this figure, and then gradually decreases for longer propagation distances. This illustrates that the beam spreads more rapidly at higher beam-order values owing to the diffraction mechanism. In other words, a laser beam with a low beam order can better withstand an increased turbulent kinetic energy dissipation rate per unit mass of the fluid.

Additionally, it has been found that when the parameter ϵ is larger and when the axial-intensity variation rate increases, the beam propagation shortens and the beam lobes expand as the turbulence intensifies. In conclusion, the analyzed beam exhibits longer propagation distances at higher spreading values of ϵ .

To investigate how wavelength affects the visible spectrum ($\lambda = 417nm$, $\lambda = 488nm$, $\lambda = 532nm$ and $\lambda = 633nm$) on studied beam's evolution characteristics using various underwater oceanic turbulence parameters (χ_T , ϵ , ζ), Several curves are presented in Fig. 7 to demonstrate the beam's normalized average intensity propagating through oceanic turbulence at a long propagation distance.

In the first few meters of the field, the normalized axial

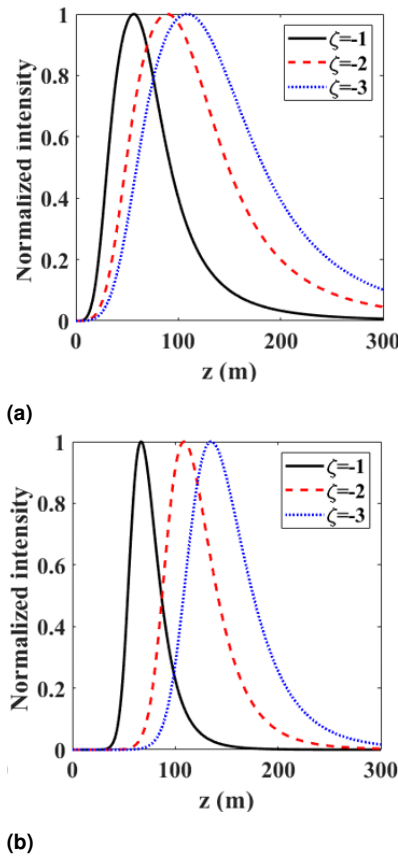


Figure 5. Normalized intensity distribution of the WGBs propagation for various values of ζ and two beam orders: (a) $s = 0$ and (b) $s = 4$, with $\epsilon = 10^{-3} \text{ m}^2 \text{ s}^{-3}$ and $\chi_T = 10^{-6} \text{ k}^2 \text{ s}^{-1}$.

intensity distribution remains unchanged; that is, as the propagation distance increases, the intensity starts to rise to its maximum value. After reaching this maximum, the intensity gradually loses its initial central dark region and begins to decrease steadily.

Furthermore, as wavelength λ increases, a broad profile is required for the average intensity distribution. Simulation studies showed that the axial intensity of the characterized beam decreases more rapidly as the beam order increases, indicating that a laser beam with a longer wavelength is better able to maintain propagation over extended distances. In turbulent media, refractive-index fluctuations mainly induce random phase distortions that scale inversely with the wavelength. Thus, longer wavelengths undergo weaker relative phase perturbations, interact less with small-scale turbulent structures, and consequently propagate more coherently, resulting in improved beam stability and increased resistance to turbulence.

By altering the beam waist ω_0 for different values of the beam-order s , we can show that Fig. 8 the intensity distribution of the propagation of the examined beam passing in oceanic turbulence as a function of z , based on Eq. 16. The figure clearly shows that as the propagation distance increases, the axial intensity also increases as well reaching its maximum value. After that, it gradually

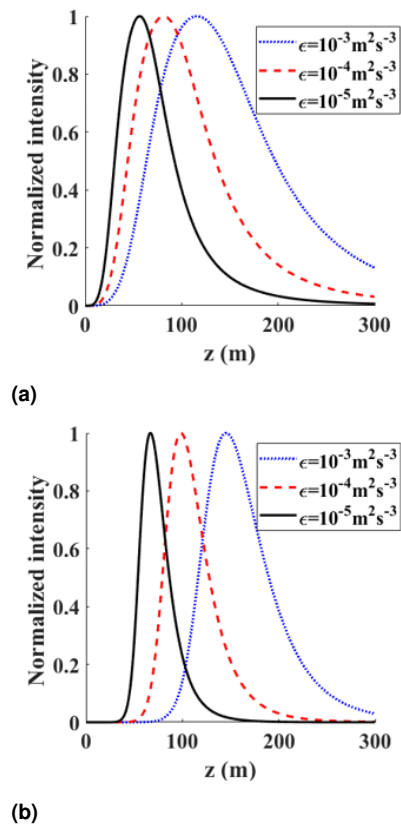


Figure 6. Normalized intensity distribution of WGBs for two different beam orders (a) $s = 0$ and (b) $s = 4$, for diverse values of ϵ , with $\zeta = -1$ and $\chi_T = 10^{-6} \text{ K}^2 \text{ s}^{-1}$.

starts to drop as the propagation distance increases. It is also apparent from these illustrations that the investigated beam intensity profile has a center dark area with zero values of the intensity and the beam waist increases with increasing beam order. Moreover, the average intensity distribution of the considered beam propagating through oceanic turbulence is significantly influenced by the beam waist width. As a result, the axial intensity lobes widen with increasing beam waist width, suggesting that the analyzed beam with modest beam waist values are more resilient to the perturbation brought on by the medium under study.

This behavior may be attributed to the fact that fluctuations in the source field increase as both the beam waist and the topological charge decrease. Additionally, increasing the beam waist can improve transmission through maritime turbulence in some cases. Physically, a larger initial beam radius reduced the intrinsic diffraction-limited confinement of the beam. Consequently, the beam interacts with a larger cross-section of turbulent eddies in the oceanic medium, making it more susceptible to phase distortions and intensity fluctuations. Conversely, a smaller waist remains more tightly confined and therefore experiences weaker cumulative turbulence effects. This explanation has now been added to the revised manuscript for clarity.

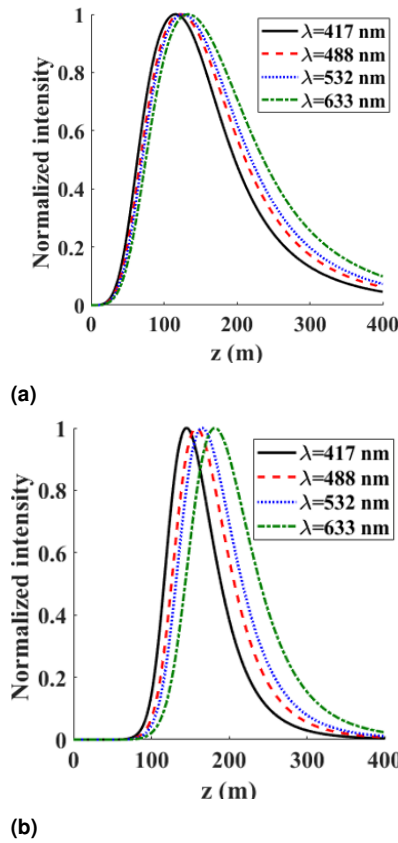


Figure 7. Normalized intensity distribution of a class of WGBs for three different values of wavelength and for two beam order values: (a) $s = 0$ and (b) $s = 4$, for diverse values of λ . The parameters that are left are $\rho_0 = 10^{-1} \text{ m}^2 \text{ s}^{-3}$, $\zeta = -1$ and $\chi_T = 10^{-6} \text{ K}^2 \text{ s}^{-1}$.

4. CONCLUSION

In this study, we theoretically analyzed the spreading of Whittaker–Gaussian beams in oceanic turbulence using the Huygens–Fresnel integral and numerical simulations of the axial intensity evolution. The results show that the turbulence resistance improves with wavelength but decreases with a larger beam radius, and the beams remain more stable under low temperature dissipation and minimal salinity fluctuations. These findings highlight the potential of Whittaker–Gaussian beams in underwater optical communication, remote sensing, and imaging. However, practical applications must consider absorption and scattering, limited range, required laser power, and experimental feasibility, as our study focused on clean water and neglected other environmental factors.

Appendix A derivation of Eq. 17

Equation 17 expresses the on-axis average intensity distribution of the Whittaker Gaussian beams propagating through oceanic turbulence, which serves as the starting

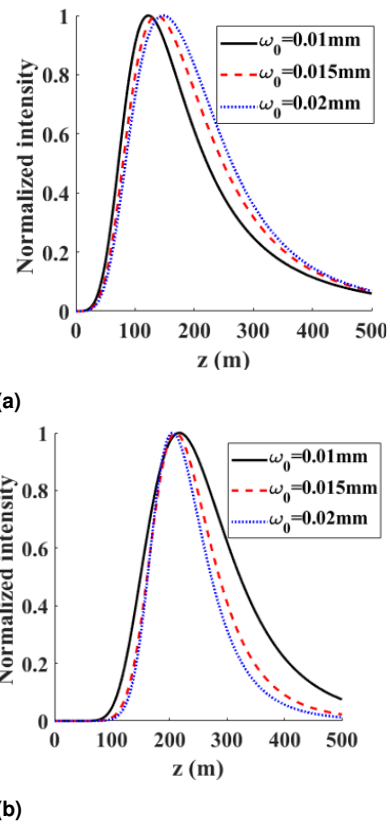


Figure 8. Normalized intensity distribution of a type of general CiBs for three different values of ω_0 and two beam-order values: (a) $s = 0$ and (b) $s = 4$, with $\rho_0 = 10^{-9} \text{ m}^2 \text{ s}^{-3}$, $\zeta = -5$ and $\chi_T = 10^{-8} \text{ K}^2 \text{ s}^{-1}$.

point for this appendix,

$$\begin{aligned} \langle I_{\text{out}}(0, z) \rangle &= \frac{k^2}{z^2} \frac{\left(\frac{1}{\rho_0^2}\right)^s}{2^2 \Gamma(s+1)} \sum_{m_1=0}^{\infty} \frac{\binom{s+1-\theta}{m_1}}{(s+1)_{m_1}} \frac{\left(\frac{i}{2\omega_0^2}\right)^{\frac{s}{2}+m_1}}{m_1!} \\ &\times \sum_{m_2=0}^{\infty} \frac{\binom{s+1-\theta}{m_2}}{(s+1)_{m_2}} \frac{\left(\frac{-i}{2\omega_0^2}\right)^{\frac{s}{2}+m_2}}{m_2!} \\ &\times \frac{\Gamma(s+m_1+1) \Gamma(s+m_2+1)}{\alpha_1^{s+m_1+1} \alpha_2^{s+m_2+1}} \\ &\times {}_2F_1\left(s+m_2+1, s+m_1+1; s+1; \frac{1}{\rho_0^4 \alpha_1 \alpha_2}\right), \end{aligned} \tag{A1}$$

where the Gaussian hypergeometric function ${}_2F_1(\cdot)$ is defined by the series representation

$$\begin{aligned} {}_2F_1\left(s+m_2+1, s+m_1+1; s+1; \frac{1}{\rho_0^4 \alpha_1 \alpha_2}\right) &= \\ \sum_{n=0}^{\infty} \frac{(s+m_2+1)_n (s+m_1+1)_n}{(s+1)_n} \times \frac{1}{n!} \left(\frac{1}{\rho_0^4 \alpha_1 \alpha_2}\right)^n, \end{aligned} \tag{A2}$$

where $(a)_n$ is the symbol for Pochhammer, using the identities listed below



$$\Gamma(s + 1 + m_1) = \Gamma(s + 1)(s + 1)_{m_1}, \tag{A3.a}$$

and

$$\Gamma(s + 1 + m_2) = \Gamma(s + 1)(s + 1)_{m_2}, \tag{A3.b}$$

and following the substitution of A2 for A1, the average intensity received is stated a

$$\begin{aligned} \langle I_{out}(0, z) \rangle &= \frac{k^2}{z^2} \frac{\left(\frac{1}{\rho_0^2}\right)^s}{4} \left(\frac{-i}{2\omega_0^2}\right)^{\frac{s}{2}} \left(\frac{i}{2\omega_0^2}\right)^{\frac{s}{2}} \frac{\Gamma(s+1)}{\alpha_1^{s+1}\alpha_2^{s+1}} \\ &\times \sum_{m_1=0}^{\infty} \sum_{m_2=0}^{\infty} \sum_{n=0}^{\infty} \frac{(s+1)_{m_1}(s+m_1+1)_n (s+m_2+1)_n (s+1)_{m_2}}{(s+1)_{m_1}(s+1)_n (s+1)_{m_2}} \tag{A4} \\ &\frac{\left(\frac{s+1-\theta}{2}\right)_{m_1} \left(\frac{s+1-\theta}{2}\right)_{m_2}}{m_1! m_2! n!} \\ &\left(\frac{i}{2\alpha_1\omega_0^2}\right)^{m_1} \left(\frac{-i}{2\alpha_2\omega_0^2}\right)^{m_2} \left(\frac{1}{\rho_0^4\alpha_1\alpha_2}\right)^n. \end{aligned}$$

Currently, by using the following

$$(s + m_1 + 1)_n = \frac{(s + 1)_{m_1+n}}{(s + 1)_{m_1}}, \tag{A5.a}$$

and

$$(s + m_2 + 1)_n = \frac{(s + 1)_{m_2+n}}{(s + 1)_{m_2}}, \tag{A5.b}$$

It is possible to rearrange Eqs. A4 as follows:

$$\begin{aligned} \langle I_{out}(0, Z) \rangle &= \frac{k^2}{z^2} \frac{\left(\frac{1}{\rho_0^2}\right)^s}{4} \left(\frac{-i}{2\omega_0^2}\right)^{\frac{s}{2}} \left(\frac{i}{2\omega_0^2}\right)^{\frac{s}{2}} \frac{\Gamma(s+1)}{\alpha_1^{s+1}\alpha_2^{s+1}} \\ &\times \sum_{m_1=0}^{\infty} \sum_{m_2=0}^{\infty} \sum_{n=0}^{\infty} \frac{(s+1)_{m_1+n} (s+1)_{m_2+n} \left(\frac{s+1-\theta}{2}\right)_{m_1} \left(\frac{s+1-\theta}{2}\right)_{m_2}}{(s+1)_n (s+1)_{m_1} (s+1)_{m_2}} \\ &\frac{1}{m_1! m_2! n!} \left(\frac{i}{2\alpha_1\omega_0^2}\right)^{m_1} \left(\frac{-i}{2\alpha_2\omega_0^2}\right)^{m_2} \left(\frac{1}{\rho_0^4\alpha_1\alpha_2}\right)^n \tag{A6} \end{aligned}$$

We are aware that [47]

$$\begin{aligned} F_3 &: F_K(\alpha_1, \alpha_2, \alpha_2, \beta_1, \beta_2, \beta_1; \gamma_1, \gamma_2, \gamma_3; x, y, z) \\ &= \sum_{h=0}^{\infty} \sum_{t=0}^{\infty} \sum_{p=0}^{\infty} \frac{(\alpha_1)_h (\alpha_2)_{t+p} (\beta_1)_{h+p} (\beta_2)_t x^h y^t z^p}{(\gamma_1)_h (\gamma_2)_t (\gamma_3)_p h! t! p!} \tag{A7} \end{aligned}$$

Next, Eq. A7 helps us since it allows us arrange the expressions in Eq. A6 as

$$\begin{aligned} \langle I_{out}(0, z) \rangle &= \frac{k^2}{z^2} \frac{\left(\frac{1}{\rho_0^2}\right)^s}{4} \left(\frac{-i}{2\omega_0^2}\right)^{\frac{s}{2}} \left(\frac{i}{2\omega_0^2}\right)^{\frac{s}{2}} \frac{\Gamma(s+1)}{\alpha_1^{s+1}\alpha_2^{s+1}} \\ &\times F_K \left\{ \frac{s+1-\theta}{2}, s+1, s+1, s+1, \frac{s+1-\theta}{2}, s+1 \right. \\ &\quad \left. ; s+1, s+1, s+1 \right. \\ &\quad \left. \frac{i}{2\alpha_1\omega_0^2}, \frac{-i}{2\alpha_2\omega_0^2}, \frac{1}{\rho_0^4\alpha_1\alpha_2} \right\}. \tag{A8} \end{aligned}$$

Finally, in the manuscript, Eq. A8; is equivalent to Eq. 16.

Declarations

Ethical Approval

This article does not contain any studies involving animals or human participants performed by any of the authors. We declare that this manuscript is original and is not currently being considered for publication elsewhere. We further confirm that the order of the authors listed in the manuscript has been approved by all authors.

Competing interests

The authors have no financial or proprietary interest in any material discussed in this article.

Authors' contributions

All the authors contributed to the conception and design of the study. All authors performed simulations, data collection, and analysis and commented on the present version of the manuscript. All authors have read and approved the final manuscript.

Funding:

No funding was received from any organization for this study.

Availability of data and materials

No dataset is used in the present study.

Consent for publication

The authors confirm that there was informed consent to publish the data contained in the article.

Consent to participate

Informed consent was obtained from all authors.

REFERENCES

- [1] S. He et al., "Propagation dynamics of abruptly autofocusing circular airy gaussian vortex beams in the fractional schrödinger equation," *Chaos, Solitons & Fractals*, vol. 142, no. 1, pp. 1–8, 2021. [Online]. Available: <https://www.sciencedirect.com/science/article/abs/pii/S0960077920308626>.
- [2] L. Zhang et al., "Tightly focusing evolution of the autofocusing linear polarized circular pearcey gaussian vortex beams," *Chaos, Solitons & Fractals*, vol. 143, no. 1, pp. 1–7, 2021. [Online]. Available: <https://www.sciencedirect.com/science/article/abs/pii/S0960077920309991>.
- [3] Z. Lin, Y. Wu, H. Qiu, X. Fu, K. Chen, and D. Deng, "Propagation properties and radiation forces of the chirped pearcey gaussian vortex beam in a medium with a parabolic refractive index," *Commun. Nonlinear Sci. Numer. Simul.*, vol. 94, no. 1, pp. 1–11, 2021. [Online]. Available: <https://www.sciencedirect.com/science/article/abs/pii/S1007570420303877>.



- [4] Y. Wu et al., “Autofocusing pearcey-like vortex beam along a parabolic trajectory,” *Chaos, Solitons & Fractals*, vol. 145, no. 1, pp. 1–6, 2021. [Online]. Available: <https://www.sciencedirect.com/science/article/abs/pii/S0960077921001338>.
- [5] N. Nossir, L. Dalil-Essakali, and A. Belafhal, “Analytical study of flat-topped beam characterization using the thermal lens method in sample liquids,” *Optik*, vol. 166, no. 1, pp. 323–337, 2018. [Online]. Available: <https://www.sciencedirect.com/science/article/abs/pii/S0030402618305163>.
- [6] N. Nossir, L. Dalil-Essakali, and A. Belafhal, “Diffraction of generalized humbert-gaussian beams by a helical axicon,” *Opt. Quantum Electron.*, vol. 53, no. 1, pp. 1–13, 2021. DOI: 10.1007/s11082-020-02662-5. [Online]. Available: <https://link.springer.com/article/10.1007/s11082-020-02662-5>.
- [7] N. Nossir, L. Dalil-Essakali, and A. Belafhal, “Introduction of besse higher-order cosh-gaussian beam and its propagation through a paraxial abcd optical system,” *Opt. Quantum Electron.*, vol. 55, no. 1, pp. 1–14, 2023. DOI: 10.1007/s11082-023-05409-0. [Online]. Available: <https://link.springer.com/article/10.1007/s11082-023-05409-0>.
- [8] N. Nossir, L. Dalil-Essakali, and A. Belafhal, “Propagation analysis of some doughnut lasers beams through a paraxial abcd optical system,” *Opt. Quantum Electron.*, vol. 52, no. 1, pp. 1–16, 2020. DOI: 10.1007/s11082-020-02444-z. [Online]. Available: <https://link.springer.com/article/10.1007/s11082-020-02444-z>.
- [9] L. C. Andrews and R. L. Phillips, *Laser Beam Propagation Through Random Medium*. Bellingham: SPIE Press, 1998.
- [10] S. M. Navidpour, M. Uysal, and M. Kavehrad, “Ber performance of free-space optical transmission with spatial diversity,” *IEEE Trans. on Wirel. Commun.*, vol. 6, no. 8, pp. 2813–2819, 2007. DOI: 10.1109/TWC.2007.06063. [Online]. Available: <https://ieeexplore.ieee.org/document/4290022>.
- [11] S. Arnon, “Underwater optical wireless communication network,” *Opt. Eng.*, vol. 49, no. 1, pp. 1–10, 2010. DOI: 10.1117/1.3280288. [Online]. Available: <https://ieeexplore.ieee.org/document/4290022>.
- [12] P. Han, “Lattice spectroscopy,” *Opt. Lett.*, vol. 34, no. 9, pp. 1303–1305, 2009. DOI: 10.1364/OL.34.001303. [Online]. Available: <https://opg.optica.org/ol/abstract.cfm?uri=ol-34-9-1303>.
- [13] H. Kaushal and G. Kaddoum, “Underwater optical wireless communication,” *IEEE Access*, vol. 4, pp. 1518–1547, 2016. DOI: 10.1109/ACCESS.2016.2558718. [Online]. Available: <https://ieeexplore.ieee.org/document/7450595>.
- [14] H. Wang and H. Chanson, “Experimental study of turbulent fluctuations in hydraulic jumps,” *J. Hydraul. Eng.*, vol. 141, no. 1, pp. 1–10, 2015. DOI: 10.1061/(ASCE)HY.1943-7900.0001010. [Online]. Available: [https://ascelibrary.org/doi/10.1061/\(ASCE\)HY.1943-7900.0001010](https://ascelibrary.org/doi/10.1061/(ASCE)HY.1943-7900.0001010).
- [15] S. M. Augustine and N. Chetty, “Experimental verification of the turbulent effects on laser beam propagation in space,” *Atmosfera*, vol. 27, no. 1, pp. 385–401, 2014. [Online]. Available: <https://www.sciencedirect.com/science/article/pii/S0187623614700372>.
- [16] S. Chib, L. Dalil-Essakali, and A. Belafhal, “Comparative analysis of some schell-model beams propagating through turbulent atmosphere,” *Opt. Quantum Electron.*, vol. 54, no. 1, pp. 1–17, 2022. DOI: 10.1007/s11082-022-03571-5. [Online]. Available: <https://link.springer.com/article/10.1007/s11082-022-03571-5>.
- [17] N. Nossir, L. Dalil-Essakali, and A. Belafhal, “Behavior of the central intensity of generalized humbert-gaussian beams against the atmospheric turbulence,” *Opt. Quantum Electron.*, vol. 53, pp. 665–678, 2021. DOI: 10.1007/s11082-021-03316-w. [Online]. Available: <https://link.springer.com/article/10.1007/s11082-021-03316-w>.
- [18] L. Dalil-Essakali, N. Nossir, and A. Belafhal, “Axial intensity of besse higher-order cosh-gaussian beam propagating in a turbulent atmosphere,” *Opt. Quantum Electron.*, vol. 56, no. 1, pp. 1–15, 2023. DOI: 10.1007/s11082-023-05782-w. [Online]. Available: <https://link.springer.com/article/10.1007/s11082-023-05782-w>.
- [19] A. A. A. Ebrahim, M. A. Swillam, and A. Belafhal, “Atmospheric turbulent effects on the propagation properties of a general model vortex higher-order cosh-gaussian beam,” *Opt. Quantum Electron.*, vol. 55, no. 1, pp. 1–13, 2023. DOI: 10.1007/s11082-023-04576-4. [Online]. Available: <https://link.springer.com/article/10.1007/s11082-023-04576-4>.
- [20] N. Nossir, L. Dalil-Essakali, and A. Belafhal, “Maritime turbulence effect on the axis light intensity of a besse higher-order cosh-gaussian laser beam,” *Opt. Quantum Electron.*, vol. 56, pp. 364–378, 2024. DOI: 10.1007/s11082-023-06052-5. [Online]. Available: <https://link.springer.com/article/10.1007/s11082-023-06052-5>.
- [21] H. Benzehoua and A. Belafhal, “The effects of atmospheric turbulence on the spectral changes of diffracted pulsed hollow higher-order cosh-gaussian beam,” *Opt. Quantum Electron.*, vol. 50, no. 1, pp. 973–982, 2023. DOI: 10.1007/s11082-023-05205-w. [Online]. Available: <https://link.springer.com/article/10.1007/s11082-023-05205-w>.
- [22] W. Fu and H. Zhang, “Propagation properties of partially coherent radially polarized doughnut beam in turbulent ocean,” *Opt. Commun.*, vol. 304, no. 1, pp. 11–18, 2013. [Online]. Available: <https://www.sciencedirect.com/science/article/abs/pii/S003040181300343X>.
- [23] J. Zhang, J. Xie, and D. Deng, “Second-order statistics of a partially coherent electromagnetic rotating elliptical gaussian vortex beam through non-kolmogorov turbulence,” *Opt. Express*, vol. 26, no. 21, pp. 21 249–21 257, 2018. DOI: 10.1364/OE.26.021249. [Online]. Available: <https://pubmed.ncbi.nlm.nih.gov/30119429/>.
- [24] F. Chen, Q. Zhao, Y. Chen, and J. Chen, “Polarization properties of quasi-homogeneous beams propagating in oceanic turbulence,” *J. Opt. Soc. Korea*, vol. 17, no. 2, pp. 130–135, 2013. DOI: 10.3807/JOSK.2013.17.2.130.
- [25] Y. Huang, B. Zhang, Z. Gao, G. Zhao, and Z. Duan, “Evolution behavior of gaussian shell-model vortex beams propagating through oceanic turbulence,” *Opt. Express*, vol. 22, no. 15, pp. 17 723–17 734, 2014. DOI: 10.1364/OE.22.017723. [Online]. Available: <https://pubmed.ncbi.nlm.nih.gov/25089392/>.
- [26] L. Lu, P. F. Zhang, C. Y. Fan, and C. H. Qiao, “Influence of oceanic turbulence on propagation of a radial gaussian beam array,” *Opt. Express*, vol. 23, no. 3, pp. 2827–2836, 2015. DOI: 10.1364/OE.23.002827.
- [27] C. Ding, L. Liao, H. Wang, Y. Zhang, and L. Pan, “Effect of oceanic turbulence on the propagation of cosine-gaussian-correlated schell-model beams,” *J. Opt.*, vol. 17, no. 3, p. 035 615, 2015. DOI: 10.1088/2040-8978/17/3/035615. [Online]. Available: <https://iopscience.iop.org/article/10.1088/2040-8978/17/3/035615>.
- [28] Y. Li, Y. Han, and Z. Cui, “On-axis average intensity of a hollow gaussian beam in turbulent ocean,” *Opt. Eng.*, vol. 58, no. 9, p. 096 115, 2019. DOI: 10.1117/1.OE.58.9.096115.
- [29] D. Liu, G. Wang, H. Yin, H. Zhong, and Y. Wang, “Propagation properties of a partially coherent anomalous hollow vortex beam in underwater oceanic turbulence,” *Opt. Commun.*, vol. 437, pp. 346–354, 2019. DOI: 10.1016/j.optcom.2019.01.007. [Online]. Available: <https://www.sciencedirect.com/science/article/abs/pii/S0030401819300070>.

- [30] D. Liu, H. Yin, G. Wang, and Y. Wang, "Propagation of partially coherent lorentz-gauss vortex beam through oceanic turbulence," *Appl. Opt.*, vol. 56, no. 31, pp. 8785–8792, 2017. DOI: 10.1364/AO.56.008785. [Online]. Available: <https://opg.optica.org/ao/abstract.cfm?uri=ao-56-31-8785>.
- [31] Y. Ata and Y. Baykal, "Effect of anisotropy on bit error rate for an asymmetrical gaussian beam in a turbulent ocean," *Appl. Opt.*, vol. 57, no. 9, pp. 2258–2262, 2018. DOI: 10.1364/AO.57.002258. [Online]. Available: <https://opg.optica.org/ao/abstract.cfm?uri=ao-57-9-2258>.
- [32] M. Bayraktar, "Average intensity of astigmatic hyperbolic sinusoidal gaussian beam propagating in oceanic turbulence," *Phys. Scripta*, vol. 96, no. 1, pp. 1–9, 2020. DOI: 10.1088/1402-4896/abce36. [Online]. Available: <https://iopscience.iop.org/article/10.1088/1402-4896/abce36>.
- [33] F. Ye, J. Zhang, J. Xie, and D. Deng, "Propagation properties of the rotating elliptical chirped gaussian vortex beam in the oceanic turbulence," *Opt. Commun.*, vol. 426, pp. 456–462, 2018. DOI: 10.1016/j.optcom.2018.05.042. [Online]. Available: <https://www.sciencedirect.com/science/article/abs/pii/S0030401818304681>.
- [34] H. Benzehoua and A. Belafhal, "Analysis of the behavior of pulsed vortex beams in oceanic turbulence," *Opt. Quantum Electron.*, vol. 55, no. 1, pp. 684–701, 2023. DOI: 10.1007/s11082-023-04992-6. [Online]. Available: <https://link.springer.com/article/10.1007/s11082-023-04992-6>.
- [35] H. Benzehoua, F. Saad, and A. Belafhal, "A theoretical study of spectral properties of generalized chirped hermite cosh gaussian pulse beams in oceanic turbulence," *Opt. Quantum Electron.*, vol. 55, no. 1, pp. 1–14, 2023. [Online]. Available: <https://link.springer.com/article/10.1007/s11082-023-04992-6>.
- [36] N. Nossir, L. Dalil-Essakali, and A. Belafhal, "Comparative analysis of bessel higher-order cosh- and sinh-gaussian beams spreading through oceanic turbulence," *Opt. Quantum Electron.*, vol. 56, no. 1, pp. 769–787, 2024. DOI: 10.1007/s11082-024-06672-5. [Online]. Available: <https://link.springer.com/article/10.1007/s11082-024-06672-5>.
- [37] M. Lazrek, Z. Hricha, and A. Belafhal, "Propagation properties of vortex cosine hyperbolic-gaussian beams through oceanic turbulence," *Opt. Quantum Electron.*, vol. 54, no. 1, pp. 1–14, 2022. [Online]. Available: <https://www.researchsquare.com/article/rs-1054533/v1>.
- [38] F. Saad, H. Benzehoua, and A. Belafhal, "Oceanic turbulent effect on the received intensity of a generalized hermite cosh-gaussian beam," *Opt. Quantum Electron.*, vol. 56, no. 1, pp. 1–15, 2023. DOI: 10.1007/s11082-023-05582-2. [Online]. Available: <https://link.springer.com/article/10.1007/s11082-023-05582-2>.
- [39] C. Sun, X. Lv, B. Ma, J. Zhang, D. Deng, and W. Hong, "Statistical properties of partially coherent radially and azimuthally polarized rotating elliptical gaussian beams in oceanic turbulence with anisotropy," *Opt. Express*, vol. 27, no. 3, pp. 245–256, 2019. DOI: 10.1364/OE.27.00245. [Online]. Available: <https://opg.optica.org/oe/fulltext.cfm?uri=oe-27-8-A245&id=405886>.
- [40] J. Zhang et al., "Effects of the turbulent atmosphere and the oceanic turbulence on the propagation of a rotating elliptical gaussian beam," *Appl. Phys. B*, vol. 124, no. 1, pp. 1–11, 2018. DOI: 10.1007/s00340-018-7038-2. [Online]. Available: <https://link.springer.com/article/10.1007/s00340-018-7038-2>.
- [41] F. Ye, J. Xie, S. Hong, J. Zhang, and D. Deng, "Propagation properties of a controllable rotating elliptical gaussian optical coherence lattice in oceanic turbulence," *Results Phys.*, vol. 13, no. 1, pp. 1–6, 2019. [Online]. Available: <https://www.sciencedirect.com/science/article/pii/S2211379719303717>.
- [42] D. Lopez-Mago, M. A. Bandres, and J. C. Gutiérrez-Vega, "Propagation of whittaker-gaussian beams," in *Laser Beam Shaping X*, ser. Proceedings of SPIE, vol. 7430, 2009, pp. 286–293. DOI: 10.1117/12.825282.
- [43] M. A. Bandres and J. C. Gutiérrez-Vega, "Whittaker-gaussian beams," *Opt. Lett.*, vol. 33, no. 2, pp. 177–179, 2008. [Online]. Available: <https://opg.optica.org/ol/abstract.cfm?uri=ol-33-2-177>.
- [44] N. Nossir, L. Dalil-Essakali, and A. Belafhal, "Effects of weak to moderate atmospheric turbulence on the propagation properties of the whittaker-gaussian laser beam," *Opt. Quantum Electron.*, vol. 56, no. 1, pp. 189–202, 2023. DOI: 10.1007/s11082-023-05830-5.
- [45] N. Nossir, L. Dalil-Essakali, and A. Belafhal, "Propagation analysis of whittaker-gaussian laser beam in a gradient-index medium," *Opt. Quantum Electron.*, vol. 55, no. 1, pp. 1–10, 2023. DOI: 10.1007/s11082-023-05317-3.
- [46] B. Tang, K. Chen, L. Huang, X. Zhou, and X. Lang, "Radiation force acting on a rayleigh dielectric sphere produced by whittaker-gaussian beams," *Opt. & Laser Technol.*, vol. 107, pp. 239–243, 2018. [Online]. Available: <https://www.sciencedirect.com/science/article/abs/pii/S0030399217319369>.
- [47] H. M. Srivastava and H. L. Manocha, *A Treatise on Generating Functions*. New York: Halsted Press, John Wiley and Sons, 1984.
- [48] V. V. Nikishov and V. I. Nikishov, "Spectrum of turbulent fluctuations of the sea-water refraction index," *Int. J. Fluid Mech. Res.*, vol. 27, pp. 82–98, 2000. [Online]. Available: <https://www.researchgate.net/publication/282798559>.
- [49] M. Abramowitz and I. A. Stegun, *Handbook of Mathematical Functions with Formulas, Graphs, and Mathematical Tables*. U.S. Department of Commerce, 1970.
- [50] I. S. Gradshteyn and I. M. Ryzhik, *Tables of Integrals, Series, and Products*, 5th ed. New York: Academic Press, 1994.